# Nonlinear generation of negative-group-velocity Lamb waves by non-collinear mixing: Numerical and experimental investigations

Yosuke Ishii,[a] Masaaki Yamamura,[b] and Shiro Biwa

*Department of Aeronautics and Astronautics, Graduate School of Engineering, Kyoto University, Katsura, Nishikyo-ku, Kyoto 615-8540, Japan*

## ABSTRACT

Nonlinear guided-wave mixing in elastic plates with material nonlinearity, which produces scattered waves at sum and difference frequencies, has attracted significant attention for the nondestructive evaluation of early-stage damage. In previous theoretical studies, the possibility of generating negative-group-velocity Lamb waves by non-collinear mixing was indicated by perturbation analysis. This prediction was verified numerically and experimentally in the present study. In accordance with the prior theoretical framework, specific frequency pairs and intersection angles for two primary fundamental antisymmetric $A_0$ Lamb waves were selected to produce observable negative-group-velocity $S_{2b}$ and positive-group-velocity $S_1$ symmetric modes as scattered waves at a fixed sum frequency. The actual nonlinear generation of these scattered modes was confirmed through direct three-dimensional dynamic finite-element simulations and experimental measurements using an aluminum-alloy plate. In particular, it was demonstrated that the dominant scattered mode can be selectively switched between the $S_{2b}$ and $S_1$ modes, with distinct propagation directions from the mixing region, by changing the primary frequencies while maintaining a constant intersection angle. Furthermore, an examination of the relationship between the scattered-wave amplitudes and the intersection angle for a given primary frequency pair revealed that both modes exhibit their maximum amplitudes near the angles satisfying the theoretically derived resonance condition. These findings substantiate the earlier theoretical predictions and highlight the capability for adaptive manipulation of the scattered-wave propagation direction, an advantage unique to dispersive guided waves and absent in non-dispersive bulk waves.

---

[a] Author to whom correspondence should be addressed: ishii@kuaero.kyoto-u.ac.jp
[b] Current address: Yamaha Motor Co., Ltd., 2500 Shingai, Iwata, Shizuoka 438-8501, Japan

## I. INTRODUCTION

Under certain conditions, dispersive guided elastic waves can exhibit a negative group velocity (NGV), where the energy propagates in the opposite direction to the phase velocity. These modes, often referred to as backward-propagating modes in the literature, have attracted considerable attention, and their propagation characteristics have been studied in various types of waveguides, including cylinders with circular[1–3] and rectangular[4] cross sections, layers on rigid or elastic substrates,[5–7] and multilayered structures.[3,8–10]

In particular, NGV Lamb waves in a single homogeneous isotropic plate, which represents one of the simplest and most fundamental waveguide structures, have been extensively investigated theoretically,[1,11–15] numerically,[10,14,16] and experimentally.[1,14,17–22] The existence of such modes has been utilized for the nondestructive evaluation of plate thickness[23] and the beam shaping (i.e., enhancement of the on-axis amplitude and beam narrowing) of acoustic waves transmitted through the plate.[24,25] Furthermore, NGV modes have been demonstrated to lead to negative reflection at a free edge of the plate[26,27] as well as negative refraction at a step discontinuity of a plate[28] or at a butt-joint interface between two plates of dissimilar materials with the same thickness,[29] which have been subsequently applied to the focusing[27,29–32] and cloaking[30] of Lamb waves. These studies have focused on wave propagation in linear elastic plates.

In the field of ultrasonic nondestructive evaluation, nonlinear guided-wave propagation in plates with weak material nonlinearity has been investigated to characterize early fatigue damage and material degradation.[33,34] In addition to the most extensively studied second-harmonic generation during single-mode propagation in an isotropic plate,[35–40] nonlinear mixing of two modes generating scattered waves at the sum and difference frequencies of the primary waves[41–52] has attracted increasing attention in recent years. Among these studies, Li *et al.*[47] numerically analyzed the nonlinear generation of zero-group-velocity (ZGV) Lamb waves by the collinear mixing of counter-propagating Lamb or shear-horizontal waves. Mora *et al.*[48] experimentally observed a similar ZGV mode generation via non-collinear mixing (i.e., mixing at arbitrary intersection angles).

In the authors' previous work,[49,50] the generation of NGV Lamb waves by non-collinear mixing was theoretically analyzed using a perturbation approach. Notably, these studies indicated the possibility of selectively shifting the dominant scattered-wave generation between the NGV and positive-group-velocity

(PGV) modes by adjusting the primary frequencies at a fixed intersection angle or by varying the intersection angle at a fixed primary frequency pair, thereby manipulating the propagation direction of the scattered waves. A preliminary experimental study of the nonlinear generation of NGV modes was reported in a conference paper.[53] However, to the best of the authors' knowledge, numerical and systematic experimental investigations into this phenomenon have yet to be conducted. Demonstrations of these predictions would not only validate the underlying theoretical framework but also establish the physical realizability of the predicted phenomenon.

Therefore, in this study, the nonlinear generation of scattered NGV Lamb waves by non-collinear mixing was investigated numerically and experimentally. Specifically, the generation characteristics of the sum-frequency NGV symmetric $S_{2b}$ mode (following the notation in Ref. 15) and PGV symmetric $S_1$ mode due to the mixing of two fundamental antisymmetric $A_0$ modes in an aluminum-alloy plate were considered. For the NGV $S_{2b}$ mode, the energy and phase propagate in opposite directions, whereas they propagate in the same direction for the PGV $S_1$ mode. Based on the previous analysis,[49,50] primary frequency pairs that can yield observable scattered waves (i.e., those providing high excitability of the primary waves and high conversion efficiency from the primary to the scattered waves) were selected in Sec. II. For the selected frequency pairs, the theoretically predicted switching behavior of the dominant scattered-wave modes was demonstrated numerically via direct dynamic finite-element simulations in Sec. III. These features were experimentally observed in Sec. IV using the setup reported in a recent study[51] with appropriate modifications. The conclusions are presented in Sec. V.

## II. SELECTION OF PRIMARY FREQUENCY PAIRS

In Ref. 51, the frequency and mode combinations of primary and scattered waves that yield measurable scattered-wave signals were selected based on the resonance condition, the excitability of the primary waves, and the conversion efficiency from the primary to the scattered waves (see Ref. 51 for further details). Following the same procedure, the primary-frequency pairs used in the numerical analysis (Sec. III) and experimental observations (Sec. IV) are selected in this section.

Figure 1 shows the dispersion curves of Lamb waves in an aluminum-alloy plate with a thickness of 2 mm, density $\rho = 2.70 \times 10^3\ \mathrm{kg/m^3}$, and Lamé elastic constants $\lambda = 54.8\ \mathrm{GPa}$ and $\mu = 26.7\ \mathrm{GPa}$. The symmetric NGV $S_{2b}$ mode (labeled following the notation in Ref. 15) exists in the finite frequency range of $1.43\ \mathrm{MHz} < f < 1.57\ \mathrm{MHz}$, whose branch is connected to that of the symmetric PGV $S_1$ mode through the ZGV point at $f = 1.43\ \mathrm{MHz}$ and a wavenumber of $\kappa = 0.8\ \mathrm{mm^{-1}}$. This study investigates non-collinear mixing that generates scattered waves of either of these two modes at the sum frequency.

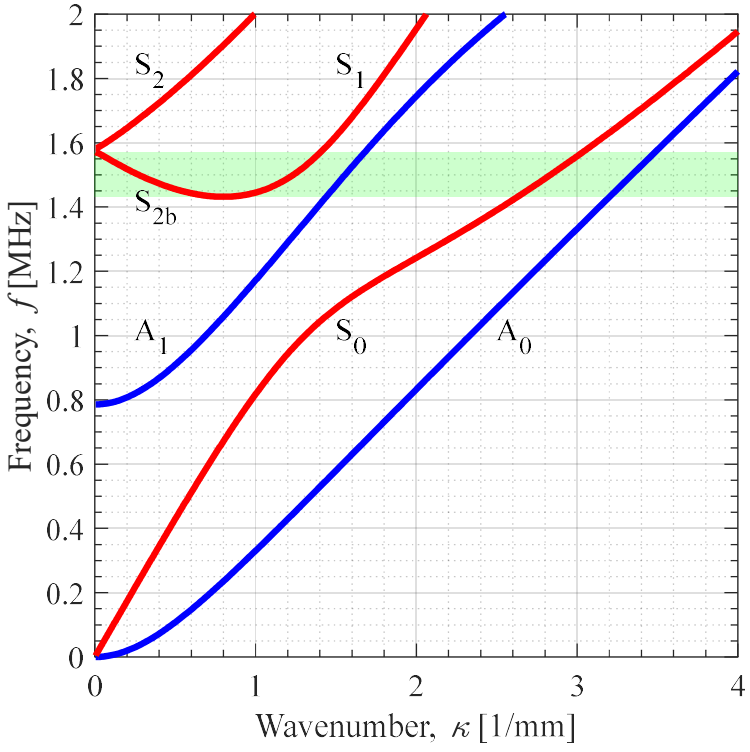



FIG. 1. Dispersion curves of Lamb waves in a 2-mm-thick aluminum-alloy plate. The frequency range in which the symmetric negative-group-velocity $S_{2b}$ mode exists is indicated by a shaded region.

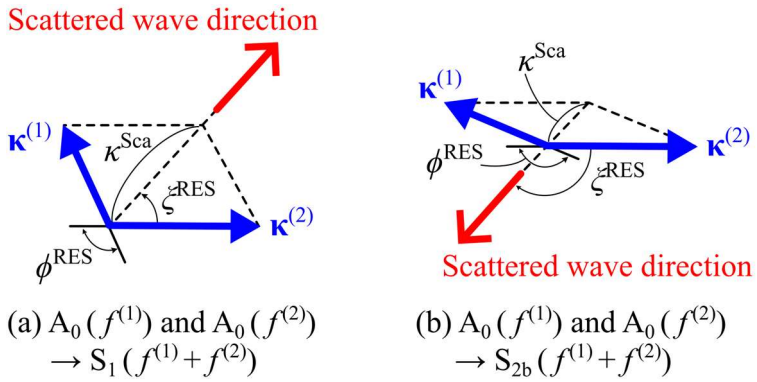
The symmetry properties of non-collinear mixing[41] indicate that scattered symmetric modes can be produced

by the mixing of two symmetric or two antisymmetric modes. In the present experiment, the primary waves are excited by piezoelectric transducers through wedges placed on the plate surface (see Sec. IV A). In view of its higher excitability[51] than the fundamental symmetric $S_0$ mode, the fundamental antisymmetric $A_0$ mode is adopted here for both primary waves. This mode pair, with a sum frequency lying within 1.43–1.57 MHz, can produce the sum-frequency scattered $S_{2b}$, $S_1$, and $S_0$ modes depending on the intersection angle, denoted by $\phi$. As the generation of the scattered $S_0$ mode has already been investigated in Ref. 51, this study focuses on the scattered $S_{2b}$ and $S_1$ modes.

According to the previous perturbation theory,[49] resonant non-collinear interactions can occur when the following resonance condition is satisfied:

$$\left\|\boldsymbol{\kappa}^{(1)} + \boldsymbol{\kappa}^{(2)}\right\| = \kappa^{\mathrm{Sca}}, \tag{1}$$

where $\boldsymbol{\kappa}^{(p)}$ $(p \in \{1, 2\})$ denotes the wavevectors of primary $A_0$ modes at frequencies $f^{(p)}$ and $\kappa^{\mathrm{Sca}}$ denotes the wavenumber of the scattered $S_{2b}$ or $S_1$ mode at the sum frequency $f^{(1)} + f^{(2)}$. As shown schematically in Fig. 2, when Eq. (1) is satisfied at the intersection angle denoted by $\phi^{\mathrm{RES}}$, the associated scattered wave is predicted to be generated predominantly in the direction of $\boldsymbol{\kappa}^{(1)} + \boldsymbol{\kappa}^{(2)}$ for the $S_1$ mode (Fig. 2(a)) and in the direction of $-\left(\boldsymbol{\kappa}^{(1)} + \boldsymbol{\kappa}^{(2)}\right)$ for the $S_{2b}$ mode (Fig. 2(b)) from the mixing region. The signed angle measured from $\boldsymbol{\kappa}^{(2)}$ to these directions is denoted by $\xi^{\mathrm{RES}}$, and is defined to be positive for the scattered $S_1$ mode.




(a) $A_0\,(f^{(1)})$ and $A_0\,(f^{(2)})$ $\rightarrow S_1\,(f^{(1)}+f^{(2)})$ (b) $A_0\,(f^{(1)})$ and $A_0\,(f^{(2)})$ $\rightarrow S_{2b}\,(f^{(1)}+f^{(2)})$

FIG. 2. Geometrical illustration of the resonance condition in Eq. (1) for the sum-frequency scattered (a) $S_1$ and (b) $S_{2b}$ modes.

The resonant intersection angle $\phi^{\mathrm{RES}}$ for the scattered $S_1$ and $S_{2b}$ modes, calculated from the dispersion relations in Fig. 1, is shown in Figs. 3(a) and 3(b), respectively, as functions of the primary frequencies in the range where $\phi^{\mathrm{RES}}$ exists for the scattered $S_{2b}$ mode within $1.43\ \mathrm{MHz} < f^{(1)} + f^{(2)} < 1.57\ \mathrm{MHz}$. Since the two primary waves are the same mode, these figures are symmetric with respect to the line $f^{(1)} = f^{(2)}$. Note that the phase velocities of the two primary waves need not be equal to each other to satisfy the resonance condition in Eq. (1), and the same applies to their group velocities. Indeed, except when $f^{(1)} = f^{(2)}$, the two primary waves in Figs. 3(a) and 3(b) generally have different phase and group velocities because of the dispersive nature of the $A_0$ mode. At a fixed $f^{(1)} + f^{(2)}$, the resonance condition is satisfied for the scattered $S_{2b}$ mode at larger values of $\phi^{\mathrm{RES}}$ in Fig. 3(b) than that for the $S_1$ mode in Fig. 3(a) due to its smaller wavenumber. In particular, as $f^{(1)} + f^{(2)}$ increases to $1.57\ \mathrm{MHz}$, the wavenumber of $S_{2b}$ mode decreases to zero (see Fig. 1), resulting in that the resonance condition can be satisfied only when $f^{(1)} \approx f^{(2)}$ at $\phi^{\mathrm{RES}} \approx 180^\circ$ as shown in Fig. 3(b).

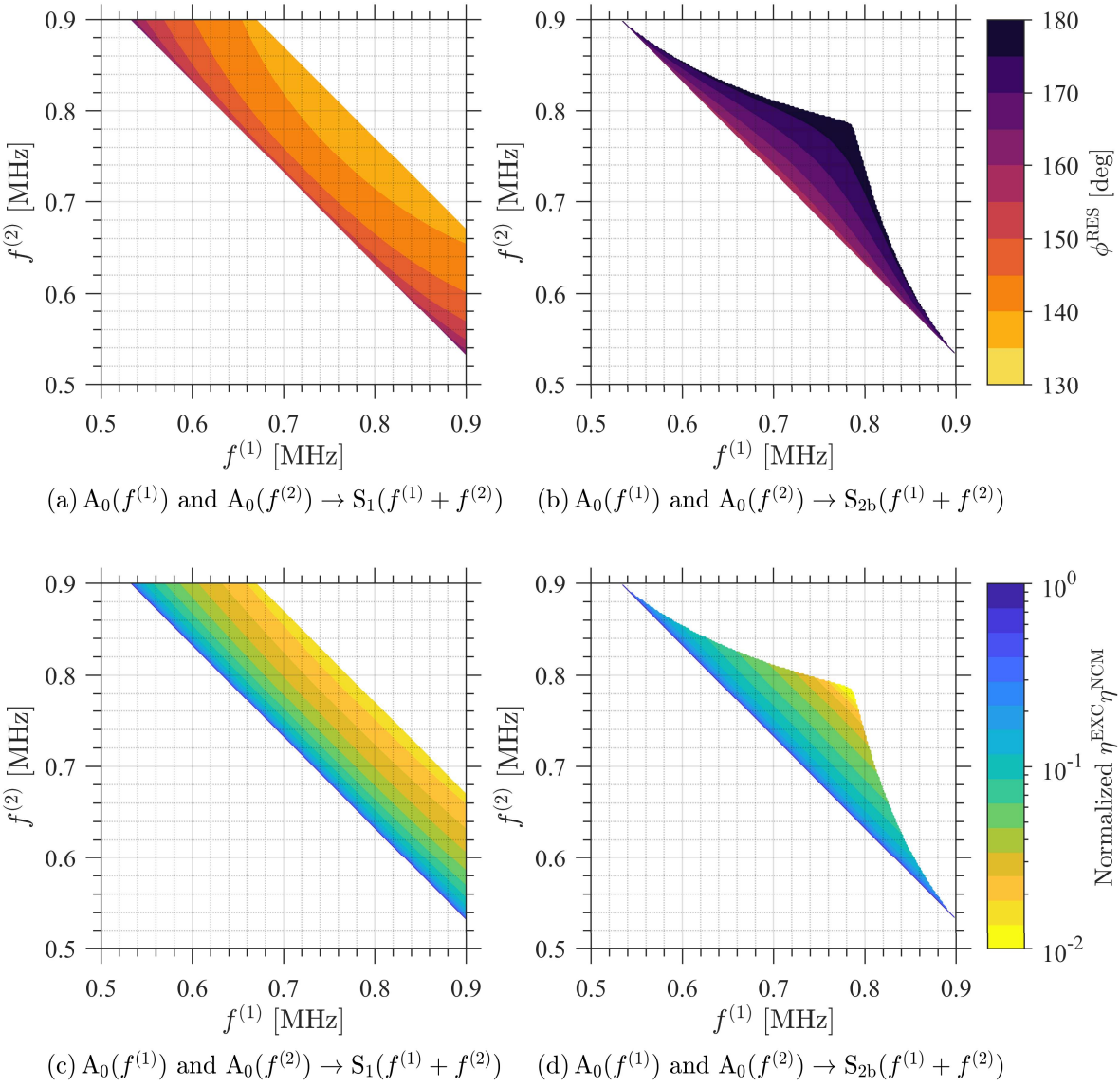



FIG. 3. Intersection angle of the primary waves $\phi^{\mathrm{RES}}$ and the normalized generation efficiency of the scattered waves at the sum frequency $\eta^{\mathrm{EXC}}\eta^{\mathrm{NCM}}$ when the resonance condition in Eq. (1) is satisfied as functions of the primary frequencies in the range of $1.43\ \mathrm{MHz} < f^{(1)} + f^{(2)} < 1.57\ \mathrm{MHz}$: (a) $\phi^{\mathrm{RES}}$ for the scattered $\mathrm{S}_1$ mode, (b) $\phi^{\mathrm{RES}}$ for the scattered $\mathrm{S}_{2\mathrm{b}}$ mode, (c) normalized $\eta^{\mathrm{EXC}}\eta^{\mathrm{NCM}}$ for the scattered $\mathrm{S}_1$ mode, and (d) normalized $\eta^{\mathrm{EXC}}\eta^{\mathrm{NCM}}$ for the scattered $\mathrm{S}_{2\mathrm{b}}$ mode. The uncolored regions correspond to $f^{(1)} + f^{(2)} \leq 1.43\ \mathrm{MHz}$, $f^{(1)} + f^{(2)} \geq 1.57\ \mathrm{MHz}$, or frequency pairs for which no intersection angle satisfies the resonance condition.

At the resonant angles in Figs. 3(a) and 3(b), a quantity representing the generation efficiency of the scattered waves[51] is evaluated; It is defined by the product of a measure of the primary wave excitability, $\eta^{\mathrm{EXC}} \equiv \left|G_{zz}^{(1)}(\mathbf{r}_1, \mathbf{r}_0)\right| \left|G_{zz}^{(2)}(\mathbf{r}_1, \mathbf{r}_0)\right|$, and that of the conversion efficiency from the primary to the scattered waves, $\eta^{\mathrm{NCM}} \equiv \left|\breve{U}_z^{\mathrm{Sca}}(\mathbf{r})\right| / \left|\breve{U}_z^{(1)}\breve{U}_z^{(2)}\right|$. Here, $z$ denotes the thickness direction and $G_{zz}^{(p)}(\mathbf{r}_1, \mathbf{r}_0)$ denotes the

contributions of the primary modes to the *zz*–component of the time-harmonic Green function for an isotropic plate (i.e., the $z$-displacement component at $\mathbf{r}_1$ in response to the time-harmonic point force with frequency $f^{(p)}$ acting at $\mathbf{r}_0$ in the $z$-direction). The quantity $\breve{U}_z^{\mathrm{Sca}}(\mathbf{r})$ denotes the $z$-displacement component of the sum-frequency scattered wave at $\mathbf{r}$, generated by the non-collinear mixing of time-harmonic straight-crested primary waves (with the $z$-displacement components $\breve{U}_z^{(p)}$ on the plate surface) within a right circular cylindrical region with a radius of $R_0$ and height equal to the plate thickness (See Ref. 51 for further details of $\eta^{\mathrm{EXC}}$ and $\eta^{\mathrm{NCM}}$). The source location $\mathbf{r}_0$ and observation location $\mathbf{r}_1$ for $\eta^{\mathrm{EXC}}$ are set on the upper plate surface and separated by a distance of $70$ mm, while the observation location $\mathbf{r}$ for $\eta^{\mathrm{NCM}}$ is set on the upper plate surface at a distance of $25$ mm from the center of the mixing region in the directions of $\boldsymbol{\kappa}^{(1)}+\boldsymbol{\kappa}^{(2)}$ and $-\left(\boldsymbol{\kappa}^{(1)}+\boldsymbol{\kappa}^{(2)}\right)$ for the $S_1$ and $S_{2b}$ modes, respectively, and $R_0 = 10$ mm. The Landau–Lifshitz third-order elastic constants of the plate are set to $\mathcal{A} = -408$ GPa, $\mathcal{B} = -197$ GPa, and $\mathcal{C} = -114$ GPa.[54] The resulting values of the product $\eta^{\mathrm{EXC}}\eta^{\mathrm{NCM}}$ are shown in Figs. 3(c) and 3(d), where the color scale is normalized by the maximum value across both figures. For both scattered wave modes, the product $\eta^{\mathrm{EXC}}\eta^{\mathrm{NCM}}$ is dominated primarily by the value of $f^{(1)}+f^{(2)}$ rather than the individual primary frequencies, and tends to increase as $f^{(1)}+f^{(2)}$ decreases to $1.43$ MHz.

With the aim of obtaining observable scattered waves as well as clearly distinguishing the scattered $S_1$ and $S_{2b}$ modes in the following numerical and experimental investigations, the present study adopts the sum frequency of $f^{(1)}+f^{(2)} = 1.45$ MHz with $f^{(1)} \leq f^{(2)}$. The corresponding wavenumbers and group velocities of the scattered modes are summarized in Table I. Figure 4 shows the profiles of $\phi^{\mathrm{RES}}$ and the normalized $\eta^{\mathrm{EXC}}\eta^{\mathrm{NCM}}$ in Fig. 3 at the selected sum frequency, together with the corresponding angles $\xi^{\mathrm{RES}}$ (see Fig. 2). As seen in Fig. 4(a), for a fixed intersection angle $\phi^{\mathrm{RES}} \gtrsim 162°$, distinct primary frequency pairs can be found that satisfy the resonance conditions for the $S_1$ and $S_{2b}$ modes, respectively. Similarly, for a fixed frequency $f^{(1)} \gtrsim 0.59$ MHz, distinct resonant intersection angles exist for the two scattered modes.

In this study, five primary frequency pairs are selected, as listed in Table II and indicated by the vertical dashed lines in Fig. 4. Cases I-P and I-N involve different frequency pairs yielding the same resonant intersection

angle of $\phi^{\mathrm{RES}} = 165^{\circ}$ for the scattered $S_1$ (Case I-P) and $S_{2b}$ (Case I-N) modes. Similarly, Cases II-P and II-N share a slightly smaller resonant intersection angle of $\phi^{\mathrm{RES}} = 163^{\circ}$. These pairs indicate that the dominant wave mode generated by non-collinear mixing may be switched by changing the exciting frequencies with a fixed arrangement of transmitters. Case III, by contrast, involves the same primary frequencies of $f^{(1)} = f^{(2)} = 0.725$ MHz resulting in different resonant intersection angles of $\phi^{\mathrm{RES}} = 146^{\circ}$ and $162^{\circ}$ for the scattered $S_1$ and $S_{2b}$ modes, respectively. This case will be adopted to investigate the intersection-angle dependence of the scattered-wave amplitudes, owing to the simple geometrical configuration of the transmitters and receivers in the experiment.

TABLE I. Wavenumber and group velocity of the sum-frequency $S_1$- and $S_{2b}$-mode Lamb waves at 1.45 MHz.

| | $S_1$ mode | $S_{2b}$ mode |
|---|---|---|
| Wavenumber, $\kappa^{\mathrm{Sca}}$ [1/mm] | 1.04 | 0.54 |
| Group velocity, $c_{\mathrm{g}}^{\mathrm{Sca}}$ [km/s] | 1.02 | −0.87 |

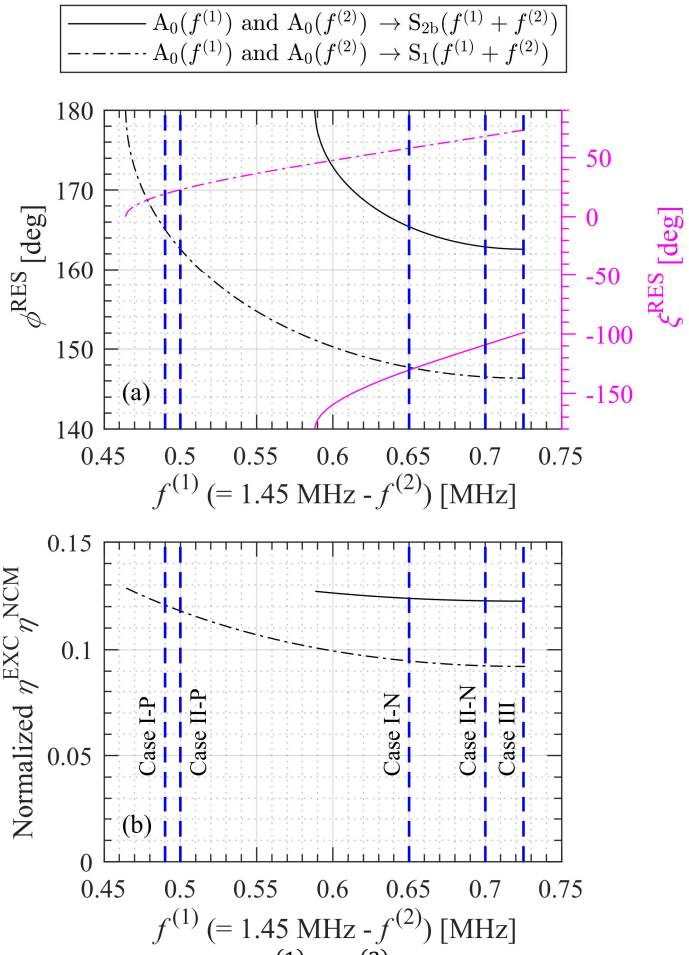



FIG. 4. Profiles of the distributions in Fig. 3 at $f^{(1)} + f^{(2)} = 1.45$ MHz, showing (a) the resonant intersection angle $\phi^{\mathrm{RES}}$ and (b) the normalized scattered-wave generation efficiency $\eta^{\mathrm{EXC}}\eta^{\mathrm{NCM}}$. The corresponding angle $\xi^{\mathrm{RES}}$, measured from $\boldsymbol{\kappa}^{(2)}$ to the predicted scattered-wave radiation direction, is plotted against the right vertical axis in (a). The primary frequencies listed in Table II are represented by vertical dashed lines.

TABLE II. Selected primary frequency pairs for non-collinear mixing of two $A_0$-mode Lamb waves to generate the sum-frequency $S_1$- and $S_{2b}$-mode Lamb waves at 1.45 MHz.

| | Primary frequencies [MHz][a] | | For sum-frequency $S_1$ mode | | For sum-frequency $S_{2b}$ mode | |
|---|---|---|---|---|---|---|
| | $f^{(1)}$ | $f^{(2)}$ | $\phi^{\mathrm{RES}}$ | $\xi^{\mathrm{RES}}$ | $\phi^{\mathrm{RES}}$ | $\xi^{\mathrm{RES}}$ |
| Case I-P | 0.49 (3.16) | 0.96 (3.16) | 165° | 21° | None | None |
| Case I-N | 0.65 (3.18) | 0.80 (3.17) | 148° | 58° | 165° | -128° |
| Case II-P | 0.50 (3.16) | 0.95 (3.15) | 163° | 23° | None | None |
| Case II-N | 0.70 (3.18) | 0.75 (3.18) | 147° | 68° | 163° | -109° |
| Case III | 0.725 (3.18) | 0.725 (3.18) | 146° | 73° | 162° | -99° |

[a] Values in parentheses indicate the corresponding group velocities (km/s).

## III. FINITE-EMELENT ANALYSIS

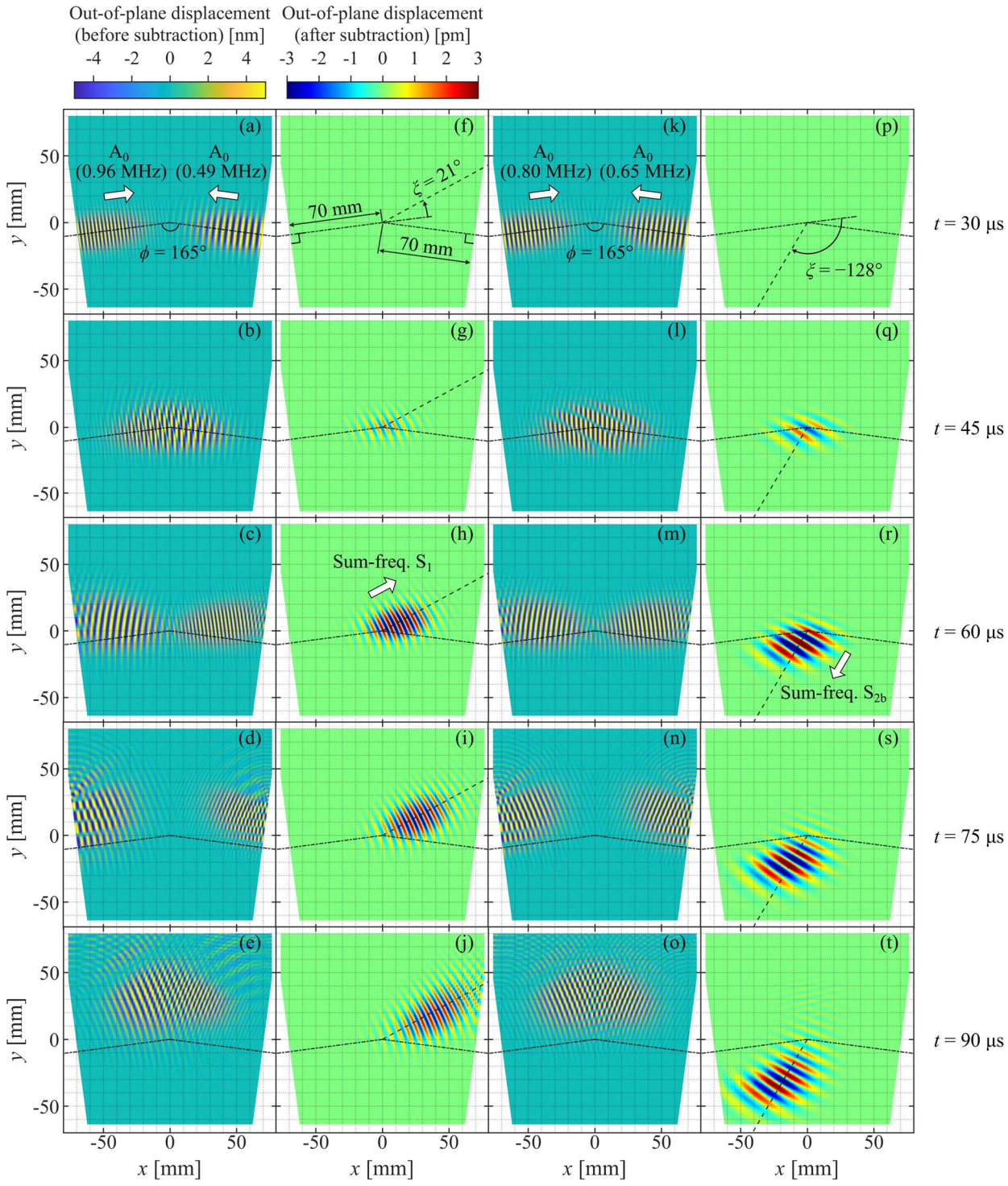
Before carrying out the experimental observations, the generation of sum-frequency $S_1$ and $S_{2b}$ modes by the non-collinear mixing of two $A_0$-mode Lamb waves is numerically examined using a three-dimensional dynamic finite-element analysis. In Ref. 51, the influence of the intersection angle between two primary $A_0$ modes on the generation of the sum-frequency $S_0$ mode was investigated using an in-house FORTRAN code in combination with the open-source code FrontISTR.[55] The present analysis follows the same finite-element procedure. A right hexagonal prism-shaped plate of 2 mm thickness is modeled as an isotropic hyperelastic solid with quadratic nonlinearity, whose density and elastic constants were given in Sec. II. The primary waves are excited by prescribing nodal displacements on the lateral surfaces of the plate, using theoretical profiles of the straight-crested $A_0$ modes in the $z$-direction with the amplitudes of the $z$-displacement components on the plate surfaces set to $10\,\mathrm{nm}$ and the Gaussian weighting with a standard deviation of $8.4\,\mathrm{mm}$ in the in-plane direction. The corresponding temporal distributions are defined as sinusoidal waves at frequencies $f^{(p)}$, modulated by a Gaussian function with a standard deviation of $7\,\mu\mathrm{s}$ and centered at $25\,\mu\mathrm{s}$ (see also Fig. 8(b)). The beam axes of the primary waves are arranged symmetrically with respect to the $y$-axis, each making an angle $\phi/2$ with it. Their intersection point, denoted by mixing point, is taken as $(x, y) = (0, 0)$. The distances from the excitation surfaces to this point are set to $70\,\mathrm{mm}$. The remaining surfaces of the plate are traction-free. For further details of the finite-element analysis procedure, see Sec. S2 of the supplementary material in Ref. 51.

Figure 5 compares the $x - y$ distributions of the $z$-displacement component on the upper surface of the plate at several representative time steps, obtained for Case I-P (Figs. 5(a)–5(j)) and Case I-N (Figs. 5(k)–5(t)) in Table II at the shared theoretical resonant intersection angle of $\phi = \phi^{\mathrm{RES}} = 165°$. In each case, the two primary waves are excited simultaneously without any time delay because the difference in their times of flight to the intersection point is negligible (approximately $0.01\,\mu\mathrm{s}$ based on the group velocities in Table II). The wavefields when both primary waves are excited are shown in Figs. 5(a)–5(e) and 5(k)–5(o), while the corresponding scattered wavefields obtained using the subtraction method are shown in Figs. 5(f)–5(j) and 5(p)–5(t). The expected beam axes of the primary waves are indicated by dash–dot lines, while those of the sum-

frequency scattered $S_1$ and $S_{2b}$ modes, whose directions are given by $\xi = \xi^{\mathrm{RES}}$ in Table II, are indicated by dashed lines. As the two primary waves start to intersect at around $t = 45\ \mu\mathrm{s}$ (Figs. 5(b) and 5(l)), the scattered waves are generated in the region around the mixing point (Figs. 5(g) and 5(q)) and subsequently propagate along the theoretically predicted directions.

Similarly, Fig. 6 shows the snapshots for the fixed primary frequency pair of Case III (i.e., $f^{(1)} = f^{(2)} = 0.725\ \mathrm{MHz}$) at the theoretical resonant intersection angles of $\phi = \phi^{\mathrm{RES}} = 146^\circ$ for the sum-frequency $S_1$ mode (Figs. 6(a)–6(j)) and $162^\circ$ for the sum-frequency $S_{2b}$ mode (Figs. 6(k)–6(t)). As predicted by theory, the scattered waves are observed to propagate along the positive and negative $y$-axis when $\phi = 146^\circ$ and $162^\circ$, respectively.

The scattered waves observed in Figs. 5 and 6 were confirmed to be the $S_1$ and $S_{2b}$ modes from their wavenumber–frequency spectra, obtained from a two-dimensional Fourier transform of the spatiotemporal distributions along the corresponding dashed lines. Note that at $t = 90\ \mu\mathrm{s}$ in Figs. 5(e), 5(o), and 6(o), the primary $A_0$ modes reflected from the lateral faces of the plate intersect again in the region around $(x, y) = (0, 30\ \mathrm{mm})$. Because the corresponding intersection angle differs from the relevant resonant angles, this second intersection does not generate significant scattered waves, as shown in Figs. 5(j), 5(t), and 6(t).




208

209 FIG. 5. Spatial distributions of the $z$-displacement component on the plate surface at different time steps,
210 obtained from a finite-element analysis for the primary frequency pairs of (a)–(j) Case I-P and (k)–(t) Case I-N
211 at an intersection angle of $\phi = 165°$. The first and third columns show the wavefields with both primary $A_0$-
212 mode Lamb waves excited, while the second and fourth columns show the corresponding wavefields after
213 applying the subtraction method. The expected beam axes of the primary and scattered waves are indicated by
214 dash–dot and dashed lines, respectively. The uncolored regions correspond to areas outside the plate.

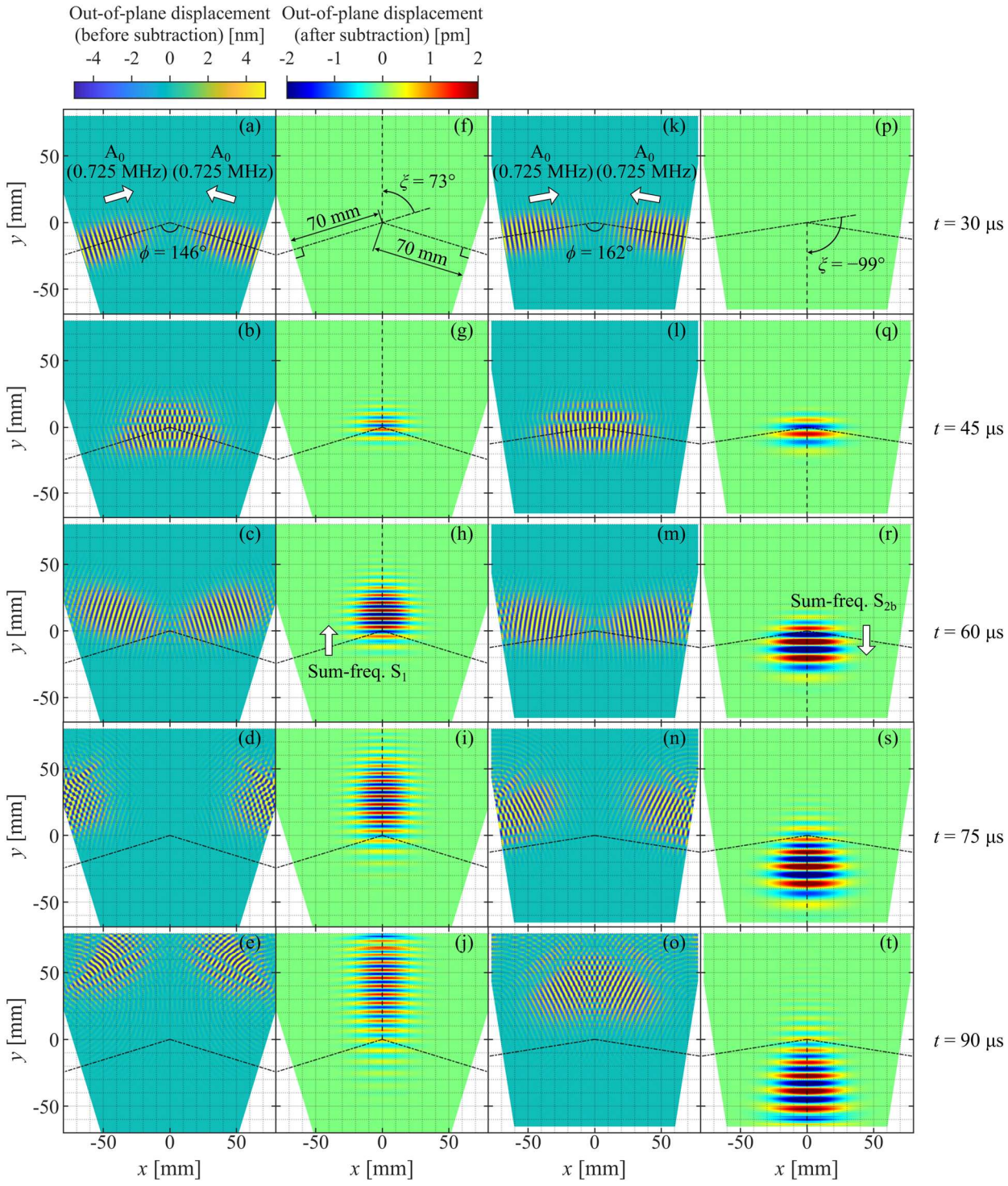



FIG. 6. The same as Fig. 5, but for the primary frequency pair of Case III at intersection angles of (a)–(j) $\phi = 146°$ and (k)–(t) $\phi = 162°$.

The finite-element simulation is now performed for Case III at different intersection angles $\phi$ ranging from $120°$ to $180°$. As shown in Fig. 6, symmetric excitation of the two identical primary waves with respect to the $y$-axis leads to sum-frequency scattered waves radiated along it, irrespective of the value of $\phi$. Accordingly, the $z$-displacement amplitude of the scattered waves is evaluated at two fixed positions: P1 at $(x, y) = (0, 25\ \text{mm})$ and P2 at $(x, y) = (0, -25\ \text{mm})$, corresponding to the main propagation directions of the scattered $S_1$ and $S_{2b}$ modes, respectively (as illustrated in the inset of Fig. 7). The results are plotted against $\phi$ in Fig. 7.

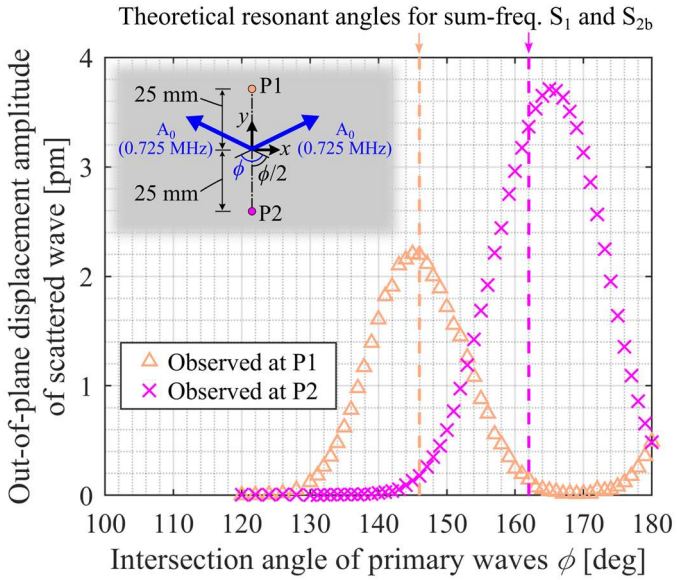



FIG. 7. Relationship between the $z$-displacement amplitude of the scattered waves evaluated at two points (denoted by P1 and P2 in the inset) and the intersection angle of the primary waves, obtained from a finite-element analysis for the primary frequency pair of Case III. The vertical dashed lines indicate the theoretical resonant intersection angles for the sum-frequency scattered $S_1$ ($\phi^{\text{RES}} = 146°$) and $S_{2b}$ ($\phi^{\text{RES}} = 162°$) modes.

Previous theoretical studies[49,50] predicted the transition between the resonant generation of PGV and NGV scattered waves by varying the intersection angle at fixed primary frequencies. This feature can be observed in Fig. 7; with increasing $\phi$ from $120°$, the $S_1$ mode is first generated dominantly and reaches its peak near the corresponding resonant angle of $\phi^{\text{RES}} = 146°$. Further increase in $\phi$ then leads to a transition of the dominant scattered mode from the $S_1$ mode to the $S_{2b}$ mode and yields the maximum amplitude near the corresponding resonant angle of $\phi^{\text{RES}} = 162°$. In particular, the $S_{2b}$ mode exhibits a larger maximum amplitude than the $S_1$ mode, which is consistent with the theoretical results in Fig. 4(b) showing that for Case III, the $S_{2b}$ mode has a

higher generation efficiency than the $S_1$ mode. For larger angles of $\phi \gtrsim 170°$, the $S_{2b}$ mode is radiated from the mixing region not only in the negative $y$-direction but also slightly in the positive $y$-direction due to the finite-beam effects of the primary waves, which introduce wavevectors in various directions. At $\phi = 180°$, which corresponds to the collinear mixing of counter-propagating primary waves and yields a symmetric wavefield with respect to the $x$-axis, the $S_{2b}$ mode is radiated equally in the $\pm y$-directions. Consequently, a relatively small scattered-wave amplitude is obtained at P1 for $\phi \gtrsim 170°$, which matches the amplitude obtained at P2 when $\phi = 180°$ in Fig. 7. Note that the non-collinear mixing at $\phi = 180° + \alpha$ (for any $\alpha > 0$) is essentially the same as that at $\phi = 180° - \alpha$ due to the isotropy of the plate. Hence, the scattered-wave amplitudes obtained at P1 and P2 for $\phi = 180° + \alpha$ are identical to those obtained at P2 and P1 for $\phi = 180° - \alpha$, respectively.

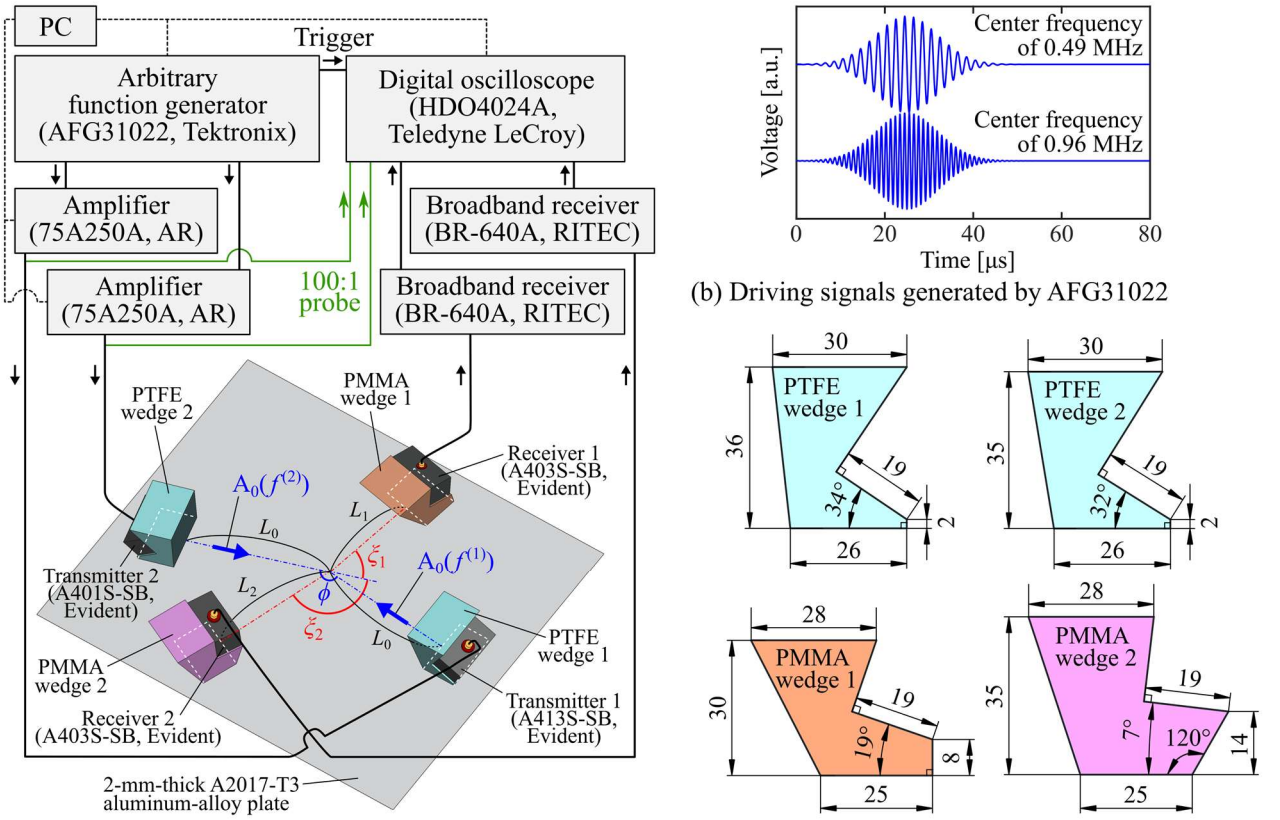
The angles at which the scattered-wave amplitudes reach their respective maxima in Fig. 7 (i.e., approximately $\phi = 145°$ and $165°$ for the $S_1$ and $S_{2b}$ modes, respectively) are slightly shifted from their resonant angles. A similar trend was observed both numerically and experimentally in the intersection-angle dependence of the sum-frequency $S_0$-mode amplitude,[51] and was suggested to arise from the transient effects of the primary waves on scattered-wave generation.[52] The slight shift observed in the present results in Fig. 7 may therefore have the same origin and does not contradict the theoretical resonance condition in Eq. (1), as the maxima still occur in the vicinity of the corresponding resonant angles.

Therefore, the results in Figs. 5–7 numerically demonstrate that the non-collinear mixing of two $A_0$-mode Lamb waves can generate the sum-frequency $S_1$ and $S_{2b}$ modes, depending on the primary frequency pair (Fig. 5) and the intersection angle (Figs. 6 and 7), as predicted by the theory in Sec. II.

## IV. EXPERIMENTS

### A. Experimental procedure

Non-collinear mixing with the primary frequency pairs listed in Table II was experimentally observed for a 2-mm-thick A2017-T3 aluminum-alloy plate, as shown schematically in Fig. 8(a). In Ref. 51, the sum-frequency $S_0$ mode generated by non-collinear mixing of two $A_0$ modes was measured using wedges and piezoelectric transducers. The experimental procedure in the present study mostly follows that described in Ref. 51 and is briefly summarized here, with particular emphasis on the differences.




(a) Setup

(b) Driving signals generated by AFG31022

(c) Wedge dimensions (Units in mm. Depth = 40 mm)

FIG. 8. Experimental setup: (a) overall configuration, (b) driving voltage waveforms for Case I-P generated by the arbitrary function generator, and (c) geometry of the transmitting and receiving wedges.

Gaussian-modulated sinusoidal voltage signals with the same waveform parameters as the excitation waveforms used in the numerical analysis in Sec. III (i.e., center frequencies $f^{(p)}$, a Gaussian standard deviation of 7 μs, and a peak location of 25 μs) were generated by an arbitrary function generator as shown in Fig. 8(b). They were then amplified to 180 $V_{pp}$ unless otherwise specified, and applied to two piezoelectric

longitudinal-wave transducers with nominal center frequencies of 0.5 MHz (Transmitter 1) and 1 MHz (Transmitter 2), with a suitable time delay such that the peak amplitudes of the excited primary waves reached the mixing point simultaneously. However, this time delay was negligibly small (approximately $0.01\,\mu s$ or less), as explained in Sec. III. Transmitters 1 and 2 were mounted on polytetrafluoroethylene (PTFE) wedges with incident angles of 34° (PTFE wedge 1) and 32° (PTFE wedge 2), as determined by Snell's law; their geometries are depicted in the top row of Fig. 8(c). PTFE was selected because its longitudinal-wave velocity (approximately 1.4 km/s) is lower than the phase velocities of the primary $A_0$ modes, allowing Snell's law to be satisfied with real incident angles. Exclusively in Case III, transducers with nominal center frequencies of 1 MHz and 32° PTFE wedges were used for both primary wave excitations.

In Ref. 51, a single pair of a polymethylmethacrylate (PMMA) wedge and a piezoelectric longitudinal-wave transducer was used to measure the sum-frequency $S_0$ mode. In contrast, the present study employed two pairs to detect the sum-frequency $S_1$ and $S_{2b}$ modes; these pairs consisted of two wedges depicted in the bottom row of Fig. 8(c) (PMMA wedges 1 and 2) and two transducers with a nominal center frequency of 2.25 MHz (Receivers 1 and 2). The angles of these wedges (i.e., 19° and 7° for PMMA wedges 1 and 2, respectively) were selected again based on Snell's law. Although Snell's law can be satisfied for the sum-frequency $S_1$ and $S_{2b}$ modes using PTFE wedges as well, PMMA, with a longitudinal-wave velocity of approximately 2.7 km/s, was selected for the receiving wedges because of its lower attenuation than PTFE.

The transmitting and receiving wedges were placed on the upper surface of the plate, as shown in Fig. 8(a), with their contact faces coupled with a liquid couplant. Notably, considering the NGV feature of the $S_{2b}$ mode, the front face of PMMA wedge 2 was oriented away from the mixing region of the primary waves (see Fig. 8(a)). The signals received by Receivers 1 and 2, digitized and transferred to a personal computer, were processed using a digital bandpass filter with band edge frequencies of 1.4 and 1.5 MHz. The subtraction method[42,51] was then applied to the resulting waveforms to isolate the signals caused by non-collinear mixing.

## B. Experimental results and discussions

### *1. Cases I and II: Different exciting frequency pairs at fixed intersection angles*

Figures 9(a) and 9(b) show the subtracted waveforms for Cases I-P and I-N, respectively, recorded by the

two receivers at the shared theoretical resonant intersection angle of $\phi = \phi^{\mathrm{RES}} = 165°$. Similarly, Figs. 9(c) and 9(d) show the waveforms obtained for Cases II-P and II-N at $\phi = \phi^{\mathrm{RES}} = 163°$. As geometrically illustrated on the right side of these figures, the angles $\xi_1$ and $\xi_2$, defining the directions of receiving PMMA wedges from the mixing point (see Fig. 8(a)), were fixed at the relevant values of $|\xi^{\mathrm{RES}}|$ in Table II. The distances between the wedges and the mixing point were set to $L_0 = 70$ mm and $L_1 = L_2 = 25$ mm.

For Case I-P (Fig. 9(a)), scattered-wave signals were detected only by Receiver 1, whereas for Case I-N (Fig. 9(b)), they were detected only by Receiver 2, consistent with the finite-element results in Fig. 5. The same switching behavior was also observed for Cases II-P (Fig. 9(c)) and II-N (Fig. 9(d)), which involve different primary frequency pairs. Based on simple geometrical considerations of the primary- and scattered-wave propagation paths in the plate using the group velocities in Tables I and II and those in the wedges (with times of flight of approximately 6 μs and 5 μs for the transmitting and receiving wedges, respectively), the peak arrival times of the scattered $S_1$ and $S_{2b}$ modes are roughly estimated to be $90 - 100$ μs. This estimate reasonably agrees with the recorded waveforms in Fig. 9.

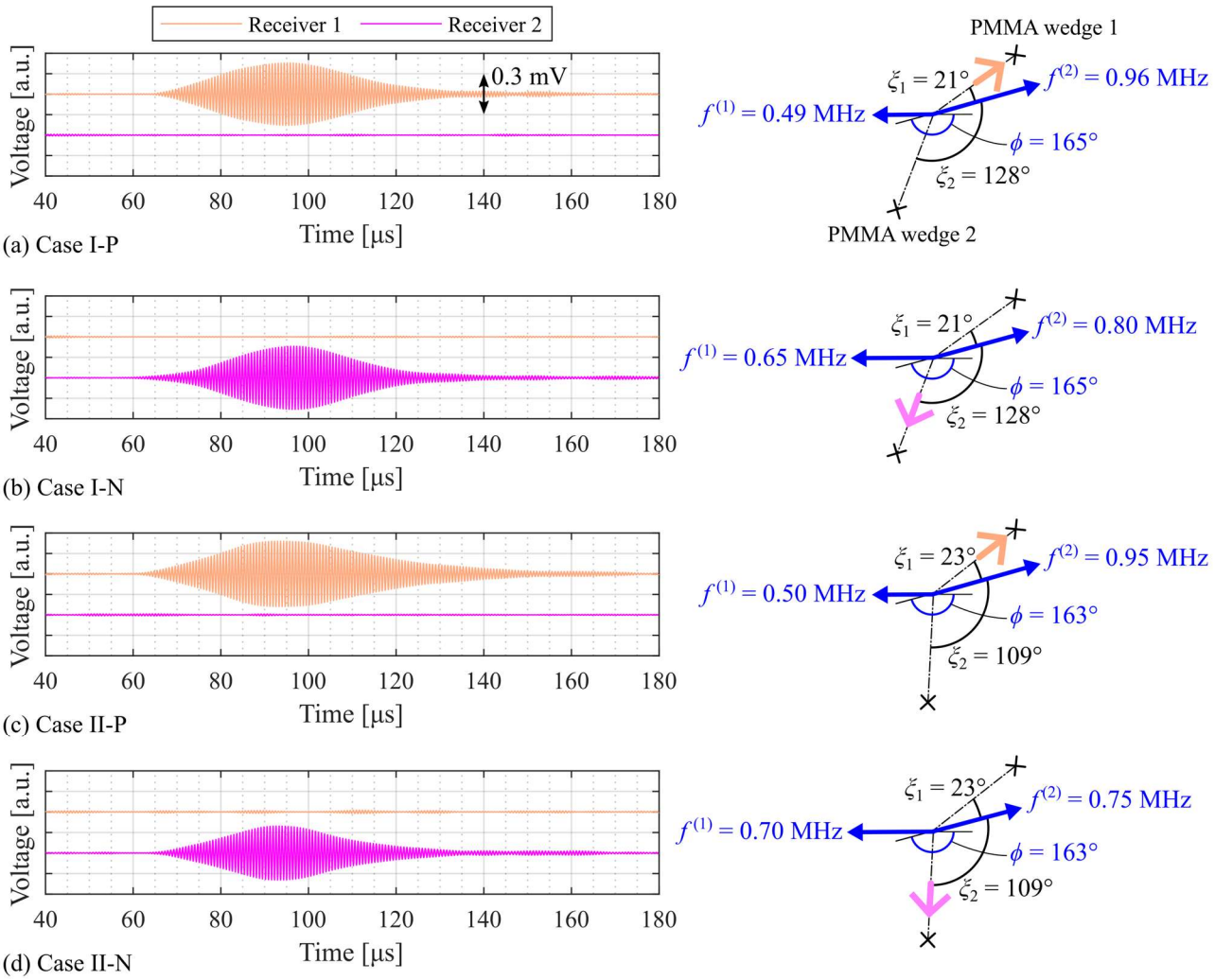



FIG. 9. Subtracted waveforms recorded by the two receivers for (a) Case I-P at $\phi = 165°$, $\xi_1 = 21°$, and $\xi_2 = 128°$, (b) Case I-N at $\phi = 165°$, $\xi_1 = 21°$, and $\xi_2 = 128°$, (c) Case II-P at $\phi = 163°$, $\xi_1 = 23°$, and $\xi_2 = 109°$, and (d) Case II-N at $\phi = 163°$, $\xi_1 = 23°$, and $\xi_2 = 109°$, with the corresponding geometrical configurations illustrated on the right.

Figure 10 shows the scattered-wave amplitudes for Case I-P (recorded by Receiver 1) and Case I-N (recorded by Receiver 2), measured for various pairs of driving voltages applied to Transmitters 1 and 2, denoted by $V^{(1)}$ and $V^{(2)}$, respectively. The scattered-wave amplitude is approximately linearly dependent on the product $V^{(1)}V^{(2)}$ for both cases. Assuming a linear response of the transducers, this implies a linear relationship between the scattered-wave displacement amplitudes and the product of the two primary-wave displacement amplitudes, a theoretically predicted feature due to quadratic material nonlinearity.[49]

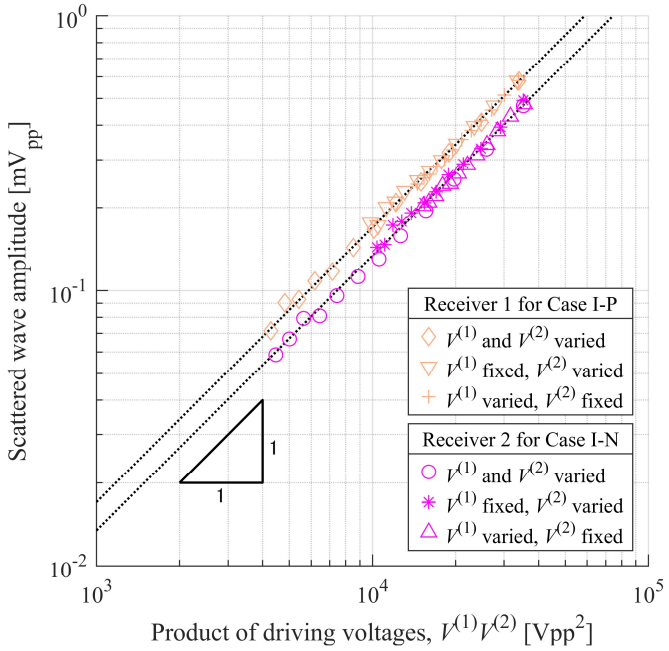



FIG. 10. Scattered-wave amplitudes plotted against the product of the driving voltages applied to the transmitting transducers for Cases I-P (recorded by Receiver 1) and I-N (recorded by Receiver 2). The corresponding geometrical configurations are identical to those shown in Figs. 9(a) and 9(b). The dotted lines represent the slopes of unity.

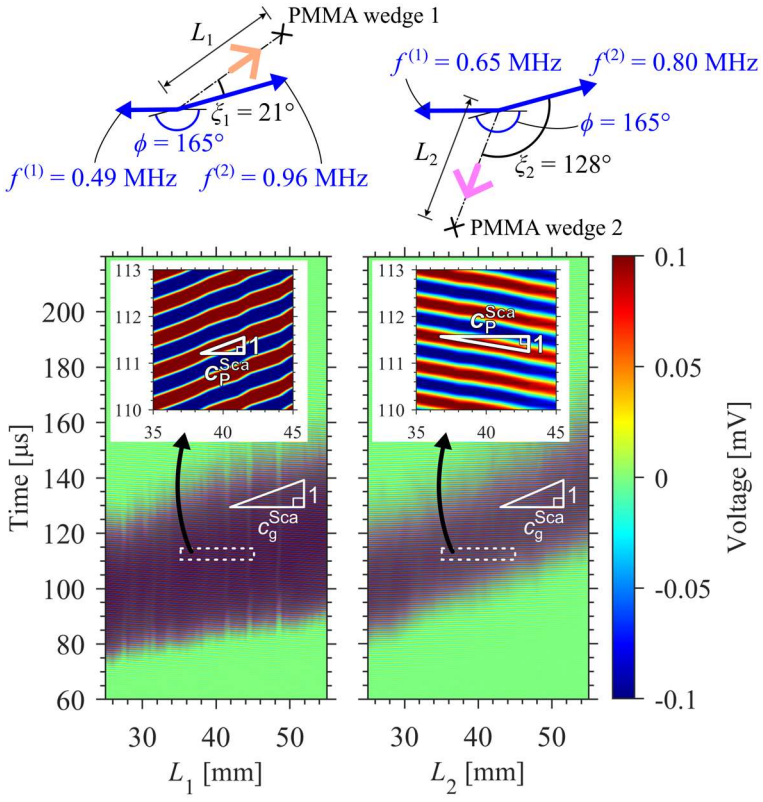
It should be noted that at all driving voltages in Fig. 10, the amplitude measured for Case I-P is larger than that for Case I-N. According to Fig. 4(b), these two cases show almost the same normalized scattered-wave generation efficiency of approximately 0.12, which alone cannot account for the observed difference in the measured amplitudes. In fact, the measured amplitudes in Fig. 10 do not provide a direct quantitative measure of the ratio of the out-of-plane displacement amplitudes of the generated scattered-wave modes, mainly because of the following two factors:

(i). Different primary-wave amplitudes: The excitability measure of the primary waves in Sec. II is defined in a simplified manner using the Green function for a point force acting on the plate surface. Therefore, it does not account for the finite-area excitation through the wedges, which may result in frequency-dependent differences in the actual amplitudes of the excited primary waves. Furthermore, in the experiments for Cases I-P and I-N, the same wedges and transducers were used to excite the primary $A_0$ modes at different center frequencies (i.e., Transmitter 1 and PTFE wedge 1 at 0.49 and 0.65 MHz, and Transmitter 2 and PTFE wedge 2 at 0.96 and 0.80 MHz). The resulting slight deviations from Snell's law

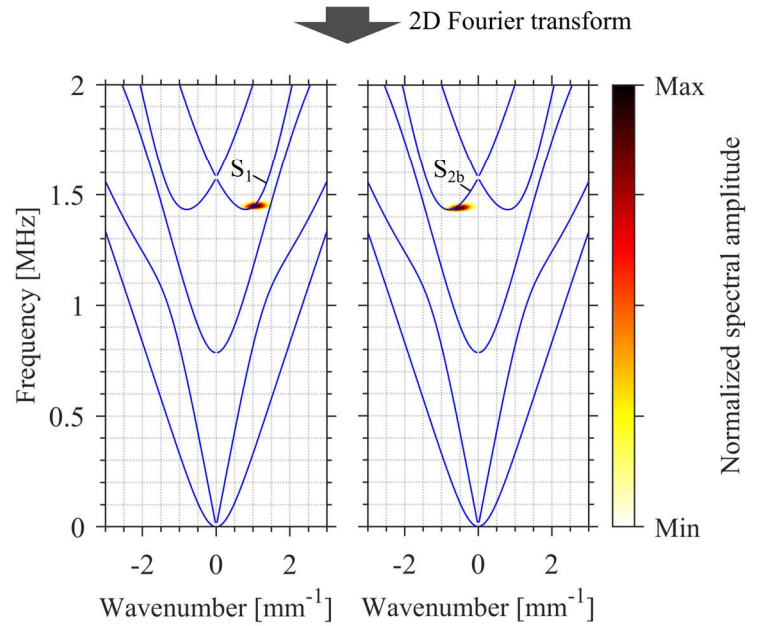
may also contribute to differences in the primary-wave amplitudes. The frequency-dependent response of each transmitting transducer may also contribute to these differences.

(ii). Different transmission efficiencies of the scattered waves from the plate into the receiving wedges: The amount of energy transmitted from the plate into a receiving wedge generally depends not only on the out-of-plane displacement but also on the normal stress associated with the corresponding scattered wave at the plate–wedge interface. Therefore, the amplitude ratio between the longitudinal waves transmitted into PMMA wedge 1 for Case I-P and PMMA wedge 2 for Case I-N does not necessarily correspond to the ratio of the out-of-plane displacement amplitudes of the two scattered Lamb-wave modes on the plate surface, as directly evaluated in the finite-element analysis in Sec. III. Furthermore, individual variability between the two receiving transducers may also affect the measured amplitude ratio.

Figure 11(a) presents the distance–time distribution of the scattered wave recorded by Receiver 1 for Case I-P at various distances $L_1$, as illustrated in the upper part of the figure. Similarly, Fig. 11(b) shows the corresponding distribution recorded by Receiver 2 for Case I-N at various distances $L_2$. In these measurements, the receiving wedges were shifted manually on the plate in 1 mm increments. Each time the wedge was moved, a weight was placed on it, and the scattered-wave signal was recorded once its waveform became stable. The slopes in Figs. 11(a) and 11(b) indicate the reciprocals of the corresponding phase velocity $c_{\mathrm{P}}^{\mathrm{Sca}}$ and group velocity $c_{\mathrm{g}}^{\mathrm{Sca}}$ of the scattered waves. These slopes have the same sign in Fig. 11(a), whereas they have opposite signs in Fig. 11(b), suggesting PGV and NGV behavior, respectively. Indeed, from the corresponding wavenumber–frequency spectra obtained from a two-dimensional Fourier transform and shown in Figs. 11(c) and 11(d), together with the theoretical dispersion curves, these scattered waves are identified as the $S_1$ and $S_{2b}$ modes, respectively. It should be noted that the horizontal axis of Fig. 11(b) is defined as the distance from the mixing point to the receiving PMMA wedge 2, assigning a positive value to the group velocity of the scattered waves. Consequently, for the NGV $S_{2b}$ mode, the slope in the inset of Fig. 11(b) is negative and its spectral amplitude peak in Fig. 11(d) appears on the branch in the negative wavenumber region.




(a) Receiver 1 for Case I-P (b) Receiver 2 for Case I-N




(c) Receiver 1 for Case I-P (d) Receiver 2 for Case I-N

FIG. 11. Spatiotemporal distributions of the scattered waves at $\phi = 165°$, recorded (a) by Receiver 1 for Case I-P with $\xi_1 = 21°$ and (b) by Receiver 2 for Case I-N with $\xi_2 = 128°$, and (c), (d) the corresponding wavenumber–frequency spectra obtained from a two-dimensional Fourier transform. The slopes in (a) and (b) correspond to the reciprocals of the group velocities $c_g^{Sca}$, whereas the slopes in the insets in (a) and (b) correspond to the reciprocals of the phase velocities $c_P^{Sca}$. The solid lines in (c) and (d) represent the theoretical dispersion curves of Lamb waves shown in Fig. 1.

Consequently, at fixed intersection angles, appropriately changing the primary frequencies can switch the generation of scattered waves between the PGV and NGV modes, as theoretically predicted.

### *2. Case III: Same exciting frequencies at different intersection angles*

Based on the results in Sec. IV B 1, the scattered waves were observed for Case III at $L_0 = 45\ \mathrm{mm}$ using a simple symmetric configuration of the transmitters and receivers with $\xi_1 = \phi/2$ and $\xi_2 = 180^\circ - \phi/2$ (see also the inset of Fig. 12 for the geometric configuration). In the same manner as in Fig. 11 for Cases I-P and I-N, the generation of the sum-frequency $S_1$ and $S_{2b}$ modes was confirmed by their wavenumber–frequency spectra measured from Receivers 1 and 2 at the theoretical resonant intersection angles of $\phi = \phi^{\mathrm{RES}} = 146^\circ$ and $162^\circ$, respectively; the obtained spectra exhibited features similar to those observed in Fig. 11, and thus are not shown here.

Figure 12 presents the scattered-wave amplitudes measured by Receivers 1 and 2 at fixed positions with $L_1 = L_2 = 25\ \mathrm{mm}$ for various intersection angles ranging from $112^\circ$ to $180^\circ$. For comparison, the finite-element results in Fig. 7 are replotted against the right vertical axis in Fig. 12. The experimental result shows reasonable qualitative agreement with the finite-element results in terms of the following points:

- Increase in the amplitudes of the $S_1$ and $S_{2b}$ modes near the corresponding theoretical resonant intersection angles indicated by the vertical dashed lines.
- Slight shift of the angles of maximum amplitudes from the resonant angles to smaller and larger values (i.e., approximately $\phi = 145^\circ$ and $166^\circ$) for the $S_1$ and $S_{2b}$ modes, respectively.

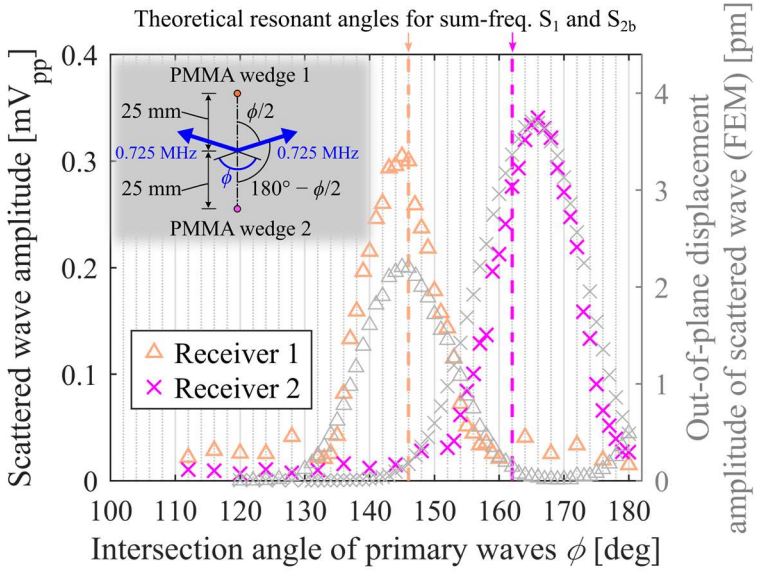



FIG. 12. Relationship between the peak-to-peak amplitudes of the sum-frequency scattered waves recorded by the two receivers and the intersection angle of the primary waves for Case III. The vertical dashed lines indicate the theoretical resonant intersection angles for the sum-frequency $S_1$ ($\phi^{\mathrm{RES}} = 146°$) and $S_{2b}$ ($\phi^{\mathrm{RES}} = 162°$) modes. Gray symbols represent the finite-element results shown in Fig. 7 and are plotted against the right vertical axis.

Although the $S_{2b}$ mode exhibits a larger maximum amplitude than the $S_1$ mode in the experimental results in Fig. 12, this difference is less pronounced than that in the finite-element results. However, the ratio between the two peak amplitudes in the experimental results cannot be directly compared with that in the finite-element results. As discussed in Sec. IV B 1 for Fig. 10, the experimentally measured amplitudes are affected by the transmission efficiencies of the scattered waves from the plate into the receiving wedges as well as individual variability between the two receiving transducers. It should be noted that the possible differences in the actual amplitudes of the excited primary waves discussed in Sec. IV B 1 do not arise in the experiments for Case III because the excitation frequencies were fixed at 0.725 MHz. Thus, the amplitude ratio measured by Receivers 1 and 2 in Fig. 12 does not directly represent the ratio of the out-of-plane displacement amplitudes of the generated $S_1$ and $S_{2b}$ modes. Furthermore, the third-order elastic constants used in the finite-element analysis were taken from the literature and were not measured for the present specimen. This can be another factor preventing a direct quantitative comparison between the experimental and finite-element results.

Therefore, the present experimental results confirmed the theoretically predicted and numerically demonstrated generation characteristics of the sum-frequency $S_1$ and $S_{2b}$ modes.

## V. CONCLUSIONS

In this study, the nonlinear generation of negative-group-velocity (NGV) Lamb waves by non-collinear mixing in an isotropic elastic plate with material nonlinearity was investigated numerically and experimentally. Based on previous theoretical analyses, frequency pairs and intersection angles for the two primary $A_0$ modes were selected to produce observable scattered NGV $S_{2b}$ and positive-group-velocity (PGV) $S_1$ modes at a fixed sum frequency. Both dynamic finite-element simulations and experimental observations confirmed the actual generation of these scattered modes by non-collinear mixing. It was demonstrated that the dominant scattered mode can be switched between the $S_{2b}$ and $S_1$ modes by selecting appropriate primary frequency pairs at a fixed intersection angle. In addition, by examining the intersection-angle dependence of the scattered-wave amplitudes at a fixed primary frequency pair, the scattered $S_{2b}$ and $S_1$ modes were shown to exhibit maximum amplitudes near their respective theoretical resonant angles. In a previous study,[51] the validity of the theoretical resonance condition was numerically and experimentally demonstrated for the scattered PGV $S_0$ mode, whereas in the present study, the validation was extended to the NGV modes.

The qualitative consistency observed among the theoretical predictions, numerical simulations, and experimental measurements confirms that the theoretical framework for non-collinear mixing established in previous studies is applicable to the NGV scattered modes. The features demonstrated in the present study, which do not occur in the non-collinear mixing of non-dispersive bulk waves,[56–58] enable the adaptive manipulation of the scattered-wave propagation direction, thereby offering potential benefits for the nondestructive damage assessment of plate-like structures using non-collinear guided-wave mixing.

## ACKNOWLEDGMENTS

This work was supported by JSPS KAKENHI Grant Number JP24K07234.

## AUTHOR DECLARATIONS

### Conflict of Interest

The authors have no conflicts to disclose.

## Author Contributions

**Yosuke Ishii:** Conceptualization (lead); software(lead); formal analysis (lead); investigation (equal); methodology (lead); visualization (lead); writing – original draft (lead); funding acquisition (lead). **Masaaki Yamamura:** Investigation (equal); methodology (supporting); writing – review and editing (supporting). **Shiro Biwa:** Writing – review and editing (lead).

## DATA AVAILABILITY

The data that support the findings of this study are available from the corresponding author upon reasonable request.

## REFERENCES


[1] A.H. Meitzler, "Backward-wave transmission of stress pulses in elastic cylinders and plates," J. Acoust. Soc. Am. **38**, 835–842 (1965).

[2] H. Cui, W. Lin, H. Zhang, X. Wang, and J. Trevelyan, "Characteristics of group velocities of backward waves in a hollow cylinder," J. Acoust. Soc. Am. **135**, 3398–3408 (2014).

[3] H. Cui, W. Lin, H. Zhang, X. Wang, and J. Trevelyan, "Backward waves with double zero-group-velocity points in a liquid-filled pipe," J. Acoust. Soc. Am. **139**(3), 1179–1194 (2016).

[4] J. Laurent, D. Royer, and C. Prada, "In-plane backward and zero group velocity guided modes in rigid and soft strips," J. Acoust. Soc. Am. **147**(2), 1302–1310 (2020).

[5] A.A. Maznev and A.G. Every, "Existence of backward propagating acoustic waves in supported layers," Wave Motion **48**(5), 401–407 (2011).

[6] T. Forbriger, L. Gao, P. Malischewsky, M. Ohrnberger, and Y. Pan, "A single Rayleigh mode may exist with multiple values of phase-velocity at one frequency," Geophys. J. Int. **222**(1), 582–594 (2021).

[7] A.A. Maznev and A.G. Every, "Surface acoustic waves with negative group velocity in a thin film structure on silicon," Appl. Phys. Lett. **95**(1), 011903 (2009).

[8] K. Nishimiya, K. Yamamoto, K. Mizutani, and N. Wakatsuki, "Negative group velocities of Lamb-type waves in a glass/water/glass structure controlled by the thickness of water layer," Jpn. J. Appl. Phys. **46**(7B), 4483–

4485 (2007).

[9] K. Nishimiya, K. Mizutani, N. Wakatsuki, and K. Yamamoto, "Relationships between existence of negative group velocity and physical parameters of materials for Lamb-type waves in solid/liquid/solid structure," Jpn. J. Appl. Phys. **47**(5), 3855–3858 (2008).

[10] T. Liu, W. Karunasena, S. Kitipornchai, and M. Veidt, "The influence of backward wave transmission on quantitative ultrasonic evaluation using Lamb wave propagation," J. Acoust. Soc. Am. **107**(1), 306–314 (2000).

[11] M.F. Werby and H. Überall, "The analysis and interpretation of some special properties of higher order symmetric Lamb waves: The case for plates," J. Acoust. Soc. Am. **111**(6), 2686–2691 (2002).

[12] I. Tolstoy and E. Usdin, "Wave propagation in elastic plates: low and high mode dispersion," J. Acoust. Soc. Am. **29**(1), 37–42 (1957).

[13] S. Cojocaru, "A parametric anomaly of the Rayleigh-Lamb spectrum in a thin elastic layer," Phys. Lett. A **483**, 129066 (2023).

[14] D.M. Stobbe and T.W. Murray, "Conical dispersion of Lamb waves in elastic plates," Phys. Rev. B **96**, 144101 (2017).

[15] P.L. Marston, "Negative group velocity Lamb waves on plates and applications to the scattering of sound by shells," J. Acoust. Soc. Am. **113**(5), 2659–2662 (2003).

[16] K. Negishi, "Existence of negative group velocities in Lamb waves," Jpn. J. Appl. Phys. **26**, 171–173 (1987).

[17] M. Germano, A. Alippi, M. Angelici, and A. Bettucci, "Self-interference between forward and backward propagating parts of a single acoustic plate mode," Phys. Rev. E **65**, 046608 (2002).

[18] A. Alippi, A. Bettucci, and M. Germano, "Conditions for anomalous acousto-optical diffraction by backward propagating acoustic waves," Phys. Rev. E **63**, 026604 (2001).

[19] B. Zaitsev, I. Kuznetsova, I. Nedospasov, A. Smirnov, and A. Semyonov, "New approach to detection of guided waves with negative group velocity : Modeling and experiment," J. Sound Vib. **442**, 155–166 (2019).

[20] J. Wolf, T.D.K. Ngoc, R. Kille, and G.M. W, "Investigation of Lamb waves having a negative group velocity," J. Acoust. Soc. Am. **83**(1), 122–126 (1988).

[21] Z. Hu, H. Cui, Z. An, and J. Mao, "Measurements of backward wave propagation using the dynamic

483 photoelastic technique," in *2016 IEEE International Ultrasonics Symposium*, (IEEE, 2016), pp. 1–4.
484 [22] K. Negishi and H.U. Li, "Strobo-photoelastic visualization of Lamb waves with negative group velocity
485 propagating on a glass plate," Jpn. J. Appl. Phys. **35**(5B), 3175–3176 (1996).
486 [23] H. Bjurström and N. Ryden, "Detecting the thickness mode frequency in a concrete plate using backward
487 wave propagation," J. Acoust. Soc. Am. **139**(2), 649–657 (2016).
488 [24] M. Aanes, K.D. Lohne, P. Lunde, and M. Vestrheim, "Finite aperture influence on energy concentration,
489 frequency shift, and signal enhancement, for acoustic transmission in the negative group velocity region of the
490 S1 leaky Lamb mode," in *2016 IEEE International Ultrasonics Symposium (IUS)*, (IEEE, 2016), pp. 1–4.
491 [25] M. Aanes, K.D. Lohne, P. Lunde, and M. Vestrheim, "Beam diffraction effects in the backward wave regions
492 of viscoelastic leaky Lamb modes for plate transmission at normal incidence," IEEE Trans. Ultrason. Ferroelectr.
493 Freq. Control **64**(10), 1558–1572 (2017).
494 [26] M. Germano, A. Alippi, A. Bettucci, and G. Mancuso, "Anomalous and negative reflection of Lamb waves in
495 mode conversion," Phys. Rev. B **85**, 012102 (2012).
496 [27] I.A. Veres, C. Grünsteidl, D.M. Stobbe, and T.W. Murray, "Broad-angle negative reflection and focusing of
497 elastic waves from a plate edge," Phys. Rev. B **93**(17), 1–8 (2016).
498 [28] F. Legrand, B. Gérardin, J. Laurent, C. Prada, and A. Aubry, "Negative refraction of Lamb modes : A
499 theoretical study," Phys. Rev. B **98**, 214114 (2018).
500 [29] C.T. Manjunath and P. Rajagopal, "Lensing in the ultrasonic domain using negative refraction induced by
501 material contrast," Sci. Rep. **9**, 6368 (2019).
502 [30] F. Legrand, B. Gérardin, F. Bruno, J. Laurent, F. Lemoult, C. Prada, and A. Aubry, "Cloaking, trapping and
503 superlensing of lamb waves with negative refraction," Sci. Rep. **11**, 23901 (2021).
504 [31] F.D. Philippe, T.W. Murray, and C. Prada, "Focusing on plates: Controlling guided waves using negative
505 refraction," Sci. Rep. **5**, 11112 (2015).
506 [32] S. Bramhavar, C. Prada, A.A. Maznev, A.G. Every, T.B. Norris, and T.W. Murray, "Negative refraction and
507 focusing of elastic Lamb waves at an interface," Phys. Rev. B Condens. Matter Mater. Phys. **83**(1), 014106
508 (2011).

509 [33] C.J. Lissenden, “Nonlinear ultrasonic guided waves - Principles for nondestructive evaluation,” J. Appl. Phys.
510 **129**(2), 021101 (2021).
511 [34] C.J. Lissenden, *Nonlinear Ultrasonic Guided Waves* (IOP Publishing, Bristol, 2024).
512 [35] M. Deng, “Cumulative second-harmonic generation accompanying nonlinear shear horizontal mode
513 propagation in a solid plate,” J. Appl. Phys. **84**(7), 3500–3505 (1998).
514 [36] M. Deng, “Cumulative second-harmonic generation of Lamb-mode propagation in a solid plate,” J. Appl.
515 Phys. **85**, 3051–3058 (1999).
516 [37] M. Deng and J. Pei, “Assessment of accumulated fatigue damage in solid plates using nonlinear Lamb wave
517 approach,” Appl. Phys. Lett. **90**, 121902 (2007).
518 [38] M.F. Müller, J.-Y. Kim, J. Qu, and L.J. Jacobs, “Characteristics of second harmonic generation of Lamb waves
519 in nonlinear elastic plates,” J. Acoust. Soc. Am. **127**(4), 2141–2152 (2010).
520 [39] N. Matsuda and S. Biwa, “Phase and group velocity matching for cumulative harmonic generation in Lamb
521 waves,” J. Appl. Phys. **109**, 094903 (2011).
522 [40] N. Matsuda and S. Biwa, “Frequency dependence of second-harmonic generation in Lamb waves,” J.
523 Nondestr. Eval. **33**(2), 169–177 (2014).
524 [41] Y. Ishii, S. Biwa, and T. Adachi, “Non-collinear interaction of guided elastic waves in an isotropic plate,” J.
525 Sound Vib. **419**, 390–404 (2018).
526 [42] M. Hasanian and C.J. Lissenden, “Second order harmonic guided wave mutual interactions in plate: Vector
527 analysis, numerical simulation, and experimental results,” J. Appl. Phys. **122**, 084901 (2017).
528 [43] W. Li, M. Deng, N. Hu, and Y. Xiang, “Theoretical analysis and experimental observation of frequency mixing
529 response of ultrasonic Lamb waves,” J. Appl. Phys. **124**, 044901 (2018).
530 [44] M. Sun, Y. Xiang, M. Deng, B. Tang, W. Zhu, and F.-Z. Xuan, “Experimental and numerical investigations of
531 nonlinear interaction of counter-propagating Lamb waves,” Appl. Phys. Lett. **114**, 011902 (2019).
532 [45] Y. Ishii, K. Hiraoka, and T. Adachi, “Finite-element analysis of non-collinear mixing of two lowest-order
533 antisymmetric Rayleigh–Lamb waves,” J. Acoust. Soc. Am. **144**, 53–68 (2018).
534 [46] M. Hasanian and C.J. Lissenden, “Second order ultrasonic guided wave mutual interactions in plate: Arbitrary

angles, internal resonance, and finite interaction region," J. Appl. Phys. **124**, 164904 (2018).

[47] W. Li, C. Zhang, and M. Deng, "Modeling and simulation of zero-group velocity combined harmonic generated by guided waves mixing," Ultrasonics **132**, 106996 (2023).

[48] P. Mora, M. Chekroun, S. Raetz, and V. Tournat, "Nonlinear generation of a zero group velocity mode in an elastic plate by non-collinear mixing," Ultrasonics **119**, 106589 (2022).

[49] Y. Ishii, T. Enoki, and S. Biwa, "Non-collinear interaction of Rayleigh–Lamb and shear horizontal waves in a finite region in a plate," Wave Motion **134**, 103488 (2025).

[50] Y. Ishii, T. Enoki, and S. Biwa, "Analysis of noncollinear mixing of guided elastic waves in a plate with material nonlinearity," in *Proceedings of the 31st International Congress on Sound and Vibration, Incheon, South Korea*, (IIAV, Auburn, AL, 2025).

[51] Y. Ishii, M. Yamamura, and S. Biwa, "Experimental observation of non-collinear mixing of fundamental antisymmetric Lamb waves," J. Acoust. Soc. Am. **159**(3), 2239–2249 (2026).

[52] Y. Ishii, M. Kato, and S. Biwa, "Nonlinear interactions of non-collinear guided wave beams in an isotropic elastic plate," J. Acoust. Soc. Am. **160**(2), 1024–1036 (2026).

[53] Y. Ishii, M. Yamamura, and S. Biwa, "Experimental study of non-collinear Lamb wave mixing due to material nonlinearity," in *Proceedings of the 32nd International Congress on Sound and Vibration, Istanbul, Türkiye*, (IIAV, Auburn, AL, 2026).

[54] R.T. Smith, R. Stern, and R.W.B. Stephens, "Third-order elastic moduli of polycrystalline metals from ultrasonic velocity measurements," J. Acoust. Soc. Am. **40**(5), 1002–1008 (1966).

[55] Information on FrontISTR is available at https://www.frontistr.com/ (last accessed September 6, 2026).

[56] G.L. Jones and D.R. Kobett, "Interaction of elastic waves in an isotropic solid," J. Acoust. Soc. Am. **35**(1), 5–10 (1963).

[57] A.J. Croxford, P.D. Wilcox, B.W. Drinkwater, and P.B. Nagy, "The use of non-collinear mixing for nonlinear ultrasonic detection of plasticity and fatigue," J. Acoust. Soc. Am. **126**(5), EL117–EL122 (2009).

[58] V.A. Korneev and A. Demčenko, "Possible second-order nonlinear interactions of plane waves in an elastic solid," J. Acoust. Soc. Am. **135**(2), 591–598 (2014).